

Chapter I

Introduction to quantum chromodynamics







I.1 Standard Model of elementary particles

One paragraph QFT







One paragraph description

One paragraph successess and drawbacks

Quarks

$2.2^{+0.5}_{-0.4} \text{ MeV}$  <i>up</i> $+\frac{2}{3}e$ 1964 - GIM mechanism	$1.28 \pm 0.03 \text{ GeV}/c^2$  <i>charm</i> $+\frac{2}{3}e$ 1974 - J/ψ meson	$172.76 \text{ GeV}/c^2$  <i>top</i> $+\frac{2}{3}e$ 1995 - Tevatron
$4.7^{+0.5}_{-0.4} \text{ MeV}/c^2$  <i>down</i> $-\frac{1}{3}e$ 1964 - GIM mechanism	$4.7^{+0.5}_{-0.4} \text{ MeV}/c^2$  <i>strange</i> $-\frac{1}{3}e$ 1964 - kaon decay	$4.7^{+0.5}_{-0.4} \text{ MeV}/c^2$  <i>bottom</i> $-\frac{1}{3}e$ 1977 - Upsilon meson

Leptons

$0.511 \text{ MeV}/c^2$  <i>electron</i> $-1e$ 1895 - X-rays	$105.66 \text{ MeV}/c^2$  <i>muon</i> $-1e$ 1936 - cosmic ray	$1.77686 \text{ GeV}/c^2$  <i>tau</i> $-1e$ 1975 - SLAC
$< 2.2 \text{ eV}/c^2$  <i>electron neutrino</i> 0 1956 - nuclear reactor	$< 0.17 \text{ MeV}/c^2$  <i>muon neutrino</i> 0 1962 - Brookhaven	$< 18.2 \text{ MeV}/c^2$  <i>tau neutrino</i> 0 2000 - Fermilab

Gauge Bosons






0  <i>photon</i> 0 1900 - Max Planck's quanta	0  <i>gluon</i> 0 1979 - PETRA	$80.379 \text{ GeV}/c^2$  W^\pm $\pm 1e$ 1983 - UA1, UA2
$91.1876 \text{ GeV}/c^2$  Z^0 0 1983 - UA1, UA2	$125.10 \text{ GeV}/c^2$  <i>Higgs</i> 0 2012 - ATLAS, CMS	

Figure 1.1: Standard model.

1.1.1 Quantum Electrodynamics

One paragraph

1.2 Coordinate systems and kinematic observables

Particles in HEP processes are described by their Lorentz-invariant four-vectors, $\mathbf{x} = (ct, x, y, z)$ and $\mathbf{p} = (E/c, p_x, p_y, p_z) = (E/c, p_T, p_z)$. In LHC experiments, the coordinate system is defined such that the x -axis points in the direction of the LHC, and the z -axis points in the direction of the beam, as shown in Fig. 1.2. In addition to the standard Cartesian coordinates, two observables, φ (azimuthal angle) and η (pseudorapidity), are used to describe the position and momentum of particles relative to the interaction point, which is located at $x = y = z = 0$. Pseudorapidity is defined as a function of the polar angle θ , where

$$\eta = -\ln(\tan(\theta/2)) \quad . \quad (1.1)$$

For high-momentum particles ($p \geq mc$), pseudorapidity is an approximation of the rapidity relative to the beam, given by

$$y = \frac{1}{2} \ln \frac{E + p_z c}{E - p_z c} \quad . \quad (1.2)$$

Rapidity is a convenient quantity to use because it transforms additively under Lorentz boosts, unlike velocity. In these coordinates, the following relations hold:

$$p_x = |\vec{p}_T| \cos \varphi, \quad p_y = |\vec{p}_T| \sin \varphi, \quad p_z = |\vec{p}| \sinh \eta. \quad (1.3)$$

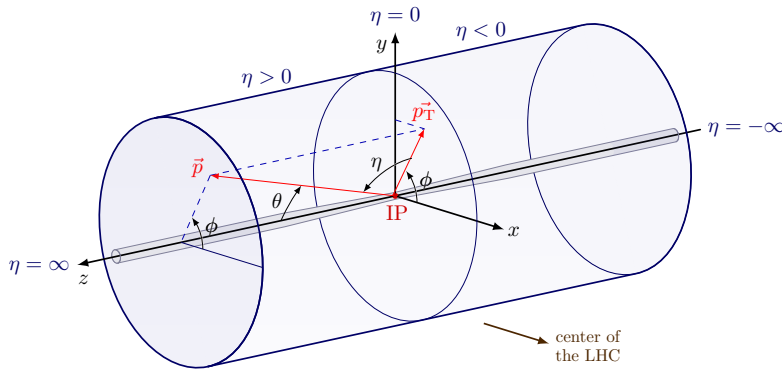


Figure 1.2: Coordinate system of an LHC experiment.

1.3 Processes involving gluons

Diagrams, screening(?), divergences

1.3.1 Running coupling constant

One paragraph, one figure

1.3.2 Perturbative QCD

One paragraph

1.4 From partons to hadrons

1.4.1 Initial and Final State Radiation

In quantum field theory, charged particles are surrounded by a cloud of virtual particles, which can be thought of as fluctuations in the particle's field. For example, the electron state can be described as a superposition of the bare electron plus additional massless bosons:

$$|e\rangle_{\text{phys}} = |e\rangle + |e\gamma\rangle + |e\gamma\gamma\rangle + \dots \quad (1.4)$$

and, at higher orders, pairs of virtual electrons. The fluctuations continuously form and recombine, with their lifetime depending on their energy and momentum. Specifically, the lifetime of a fluctuation with energy ω and transverse momentum k_T can be approximated as:

$$\tau \approx \frac{\omega}{k_T} \quad . \quad (1.5)$$

This implies that fluctuations with smaller- k_T live longer.

As illustrated in Fig. 1.3, the coherent mixed state of the bare charge and the field fluctuations can be disturbed by the presence of an interaction. Intuitively, this interaction can change the energy and momentum of the fluctuations, their formation and recombination, and lead to the emission of radiation in two ways:

1. a fluctuation is kicked on-shell by the interaction and part of the field continues in its original direction, which leads to Initial State Radiation (ISR);

2. as a result of the field of the scattered particle rearranging itself, which can be a source of Final State Radiation (FSR).

In both of the cases, a larger momentum transfer implies more radiation. *For hard, wide angle emissions, cross sections can be calculated perturbatively at fixed orders.*

Soft and collinear emissions, however, lead to infra-red divergences ($\propto \frac{1}{\omega}, \propto \frac{1}{k_T^2}$) and thus, need to be factorised away from the amplitudes or the cross sections and then described using resummation techniques. Without any emissions, the probabilities of finding electrons and photons of fractional momentum x with respect to the whole system are:

$$f_e(x) = \delta(1-x), \quad f_\gamma(x) = 0, \quad (\text{I.6})$$

When considering the emissions above some scales parametrised by the resolution parameter Q^2 , these probabilities, however, evolve according to the DGLAP equation:

$$\frac{\partial}{\partial \ln Q^2} \begin{pmatrix} f_e(x, Q^2) \\ f_\gamma(x, Q^2) \end{pmatrix} = \frac{\alpha_{\text{em}}}{2\pi} \int_x^1 \frac{dz}{z} \begin{pmatrix} P_{ee}(z) & P_{e\gamma}(z) \\ P_{\gamma e}(z) & P_{\gamma\gamma}(z) \end{pmatrix} \begin{pmatrix} f_e\left(\frac{x}{z}, Q^2\right) \\ f_\gamma\left(\frac{x}{z}, Q^2\right) \end{pmatrix}, \quad (\text{I.7})$$

where $P_{ij}(z)$ are the splitting probability functions of a particle i emitting a particle j .

In QCD, the behaviour is analogous, with $\alpha_{\text{em}} \rightarrow \alpha_s$, $e \rightarrow q$, and $\gamma \rightarrow g$.

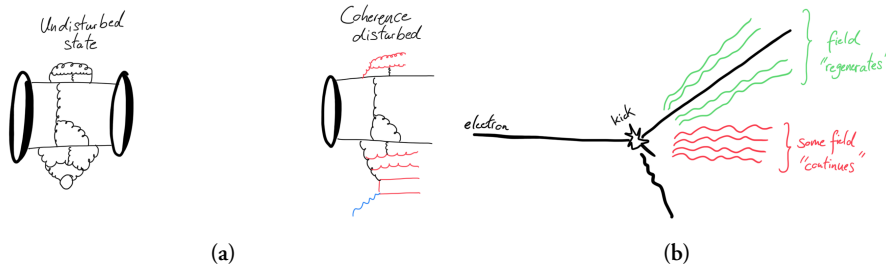


Figure 1.3: Illustration of the field fluctuations and emissions of radiation in a scattering process.

1.4.2 Factorisation theorem

The evolution equations 1.7 imply that the probabilities of observing emissions with a fractional momentum x depend on the resolution Q^2 . In QCD,

1. when applied to the initial state, they are known as parton distribution functions (PDFs) and determine the probabilities of finding partons¹ in the composite hadronic state.
2. When applied to the final state, they are called fragmentation functions, and determine the probabilities of measuring fragments of the outgoing particles.

This leads to the factorisation theorem for processes involving collisions of two hadrons, which separates the perturbatively calculable partonic cross section from the non-perturbative partonic evolution and hadronisation. The theorem can be expressed as follows:

$$\sigma = f_i^A(x_i, \mu_F) f_j^B(x_j, \mu_F) \otimes \hat{\sigma}_{ij \rightarrow n}(\mu_F, \mu_R) \otimes D_{n \rightarrow n'} . \quad (1.8)$$

Here, i and j are the initial partons, $\hat{\sigma}_{ij \rightarrow n}$ is the partonic cross section, $D_{n \rightarrow n'}$ is the process-specific fragmentation function for evolving the partons n into the particles' final state n' , and μ_F and μ_R are the factorisation and renormalisation scales, respectively. The factorisation scale, μ_F , determines the scale below which the emissions are absorbed into the PDFs. The theorem is depicted in Fig. 1.4.

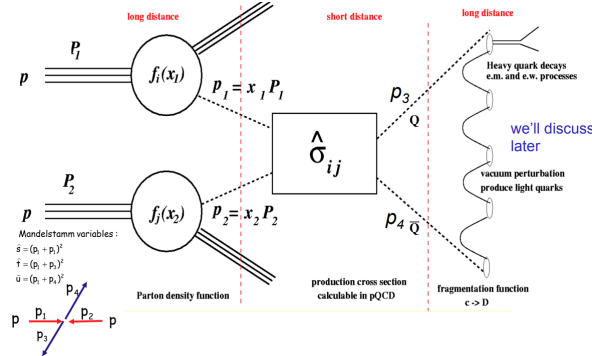


Figure 1.4: Illustration of the factorisation theorem. (NEEDS TO BE REMADE).

1.4.3 Parton distribution functions

The PDFs defining the probabilities of finding quarks and gluons in nucleons can be determined experimentally at hadron-electron colliders such as HERA. They are determined from measurements of deep inelastic scatterings in a range of energies and momentum transfers. They are displayed in Fig. 1.5 as a function of the fractional momentum x (also called Björken x).

¹Partons refer to the valence quarks, sea quarks, and gluons inside hadrons.

According to collider kinematics, $x \propto \frac{1}{\sqrt{s}}$, therefore, the partonic composition of ultra-relativistic hadrons is dominated by gluons. Following unitarity principles and BK evolution equation, it is expected that gluons start recombining and the gluonic content saturates as $x \rightarrow 0$. This is actively researched, however, not directly measured yet. Additionally, it should be noted that in ultra-relativistic heavy nuclei, the partons are modified in the contracted nuclear environment and the PDFs are referred to as nPDFs.

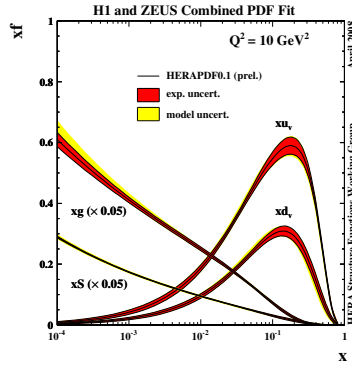


Figure 1.5: Parton distribution functions determined at HERA. TBA

1.4.4 Parton fragmentation and the Lund string

After the scattering process, the produced partons continue to fragment by emitting more partons in a process called the parton shower. Since the coupling strength in QCD increases with decreasing the energy scale of the splitting, this leads to the production of many soft, collimated emissions known as jets. The partonic evolution continues until the virtuality of the partons reaches the hadronization scale ($\approx \Lambda_{\text{QCD}}$). There are multiple frameworks within QCD to describe the evolution of partons into their final state, such as using the DGLAP equations or the so-called dipole formalism.

Once the partonic final state is reached, the partons hadronise into the observable mesons and baryons. The hadronisation process is not calculable in QCD and requires phenomenological models to describe it. One such model is the Lund String model, which describes hadronisation as the breaking of a color string between the quarks in the final state. In this model, the energy stored in the color string is converted into the mass of new hadrons.

According to confinement, hadronisation should involve at least two partons with

complementary colours. In QCD, the $q\bar{q}$ potential takes the shape of

$$V_{q\bar{q}} \approx -\frac{4}{3} \frac{\alpha_s \hbar c}{r} + \kappa r \quad , \quad (1.9)$$

where κ is a parameter with value around 1 GeV/fm. In the non-perturbative regime (long distances), the potential is dominated by the linear part, which is reminiscent of a system bound by a string with tension κ . This is taken advantage of by the Lund string model – a q and \bar{q} pair separated by distance Δx is bound by a color field (string) with energy $\kappa \Delta x$.

If the q and \bar{q} continue separating as a result of the scattering, the energy stored in the color field increases. At some point, it can become energetically favourable to produce a new $q\bar{q}$ pair out of vacuum, which is a quantum mechanics tunnelling phenomenon characterised by the probability:

$$\frac{dP}{dm_T} \propto \exp \left(-\frac{\pi m_T^2}{\kappa} \right) \quad , \quad (1.10)$$

where m_T is the transverse mass of the produced quarks. Otherwise, the $q\bar{q}$ system starts contracting and oscillates with a period $T = 2E_{\text{kin}}/\kappa$, where E_{kin} is its maximum kinetic energy. The produced q and \bar{q} then connect by new color fields to the original pair. This process repeats itself result in cascade of many $q\bar{q}$ pair connected by many color strings. In this descriptions, baryons can also be created by double tunnelling of a $qq\bar{q}\bar{q}$ pair. The process is illustrated in Fig. ??.

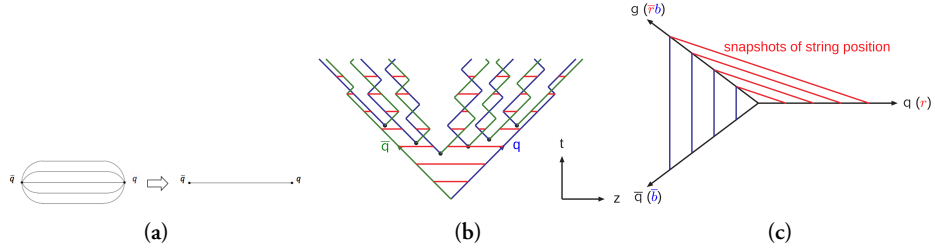


Figure 1.6: Illustration of the color field between two quarks and its simplified representation with a string. Illustration of the string splitting by producing new $q\bar{q}$ in the t - z plane. Illustration of the treatment of gluons in the Lund string model.

Equation 1.10 also implies that production of strange quarks is suppressed by a factor of

$$\rho = \exp \left(-\frac{\pi(m_s^2 - m_{u,d}^2)}{\kappa} \right) \quad . \quad (1.11)$$

This parameter is typically tuned to data, as substituting constituent ($m_s \approx 0.5 \text{ GeV}/c^2$, $m_{u,d} \approx 0.33 \text{ GeV}/c^2$) versus current masses ($m_s \approx 0.1 \text{ GeV}/c^2$, $m_{u,d} \approx 0$) leads to considerable differences underestimating and overestimating data, respectively.

For a $q\bar{q}g$ system, in this model, the gluon connects to the quark and antiquark and is effectively treated as a “kink” on the color field, adding energy and momentum to the $q\bar{q}$ string (stretching it in its direction), as visualised in Fig. ??.

It should be noted that in the paradigm of AA collisions, hadron production can be alternatively modelled by hadronisation at the QGP’s phase boundary by *coalescing* free quarks.

TBA a sentence about the actual hadronisation.

1.5 Lattice QCD

One paragraph

1.6 QCD phase diagram

One paragraph, figure

1.6.1 Phase transition

One paragraph, bag model derivation of T

1.6.2 Chiral symmetry restoration

One paragraph, figure

1.7 Implications

One paragraph

Chapter 2

QCD phenomena in high energy hadronic collisions

2.1 Collisions of heavy nuclei

2.1.1 Collision geometry, Centrality, multiplicity

Collisions of heavy nuclei, composed of many fluctuating nucleons, may occur under various initial state configurations. Some quantities used to describe them are the impact parameter b , defined as the distance between the two nuclei centers, number of participating (scattered) nucleons N_{part} , and the number of binary nucleonic collisions N_{coll} .

Determining these quantities is important because:

1. Soft processes, such as light flavor particle production, are expected to scale with the interaction volume, which $\propto N_{\text{part}}$.
2. Hard processes, such as jet and heavy flavor production, are expected to scale with the number of large momentum transfer interactions given by N_{coll} .
3. b , disregarding the fluctuations of nucleonic positions, defines the shape and anisotropy of the overlap region, which are important initial state conditions.

Since these quantities cannot be directly measured, they need to be modelled. The charged particle *multiplicity* is commonly used for this purpose, as $\langle N_{\text{ch}} \rangle$ increases

monotonically with N_{part} , N_{coll} , and decreasing b . Multiplicity N_{ch} can be measured experimentally, e.g. with tracking detectors. The concept of *centrality* is also used, which is defined as quantiles of the total nuclear cross-section. For example, a centrality of 0 – 5% refers to low b values and the top 5% of N_{ch} values (central events), while 95 – 100% centrality refers to high b values and the bottom 5% of N_{ch} values (peripheral events). Centrality can also be inferred from other *event activity* classifiers, such as amplitudes of scintillators at forward rapidity, transverse energy in calorimeters, or energy from beam remnants in zero-degree-calorimeters.

In AA collisions, these relationships are well-defined, and thus the models perform well. The most popular model is the MC Glauber model. Other models include MC-KLN and IP Glasma.

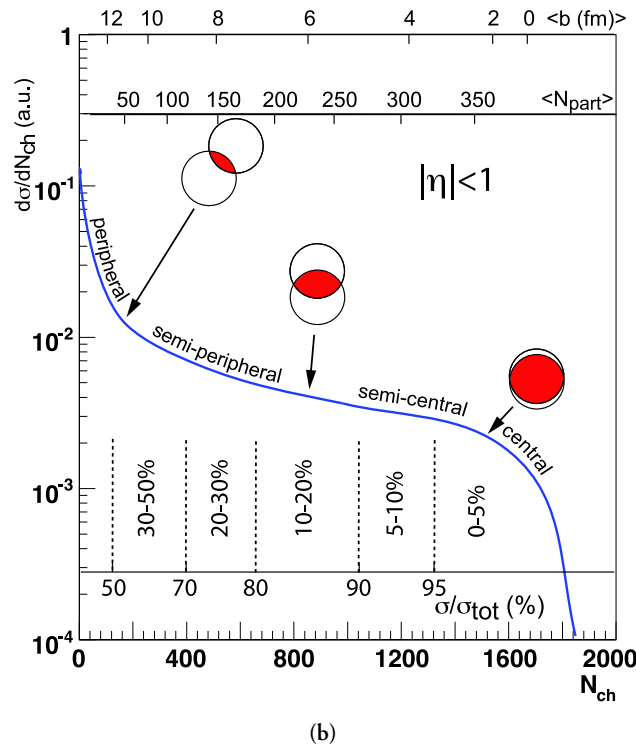
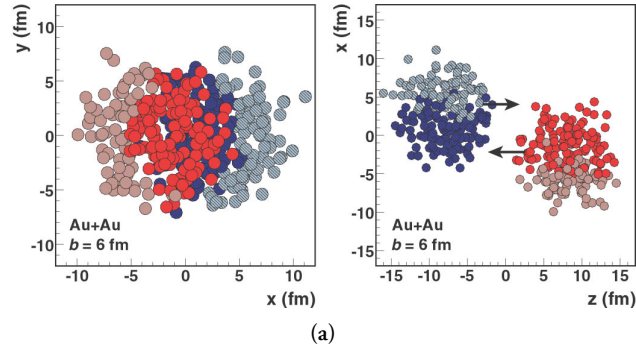
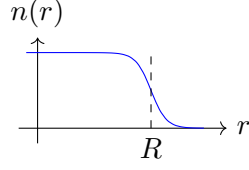


Figure 2.1: TBA

2.1.2 MC Glauber model

The MC Glauber model takes on a very simple albeit powerful approach. The two nuclei are simulated in three dimensions in a way that satisfies their respective nuclear density profiles, usually modelled by sampling the positions of nucleons from the Wood-Saxon distribution:



$$n(r) = \frac{1}{1 + \exp((r - R)/a)} \quad , \quad (2.1)$$

where R is the nuclear radius and a the nuclear skin thickness.

The nucleonic densities can be represented by uniform disks, or more accurately by Fermi-distributions or Gaussian profiles to account for fluctuations of their densities. Their parameters are left free and are tuned to the data.

A random impact parameter is then chosen or sampled. The collision is then treated as a sequence of independent binary nucleon-nucleon collisions, where

1. nucleons remain travelling in straight lines,
2. the inelastic nucleon-nucleon cross section σ_{NN} does not depend on the number of interactions,
3. two nucleons are considered to interact if their transverse relative distance $d \leq \sqrt{\sigma_{\text{NN}}/\pi}$.

Fig. 2.1 illustrates an example of a Glauber Monte Carlo event for a Au+Au collision. By simulating numerous collisions, the average N_{part} and N_{coll} are determined¹, and their relations to centrality and event activity observables are determined by fitting to experimental data.

Recent studies have extended the MC Glauber model to include sub-nucleonic structures. Such efforts show that the production of charged hadrons at mid-rapidity scales linearly with the number of participating partons. Comparisons with LHC data at $\sqrt{s_{\text{NN}}} = 5.02 \text{ TeV}$ suggest that the number of sub-nucleonic degrees of freedom ranges from 3 to 5? .

2.2 Quark-gluon plasma

In agreement with lattice QCD predictions, the QGP has been measured in ultra-relativistic collisions of heavy nuclei at RHIC? , LHC? , and even SPS? . Although it

¹It also shows the scaling between the numbers of participants and binary collisions, which is approximately $N_{\text{coll}} \approx 0.35 N_{\text{part}}^{4/3}$.

cannot be observed directly, a wealth of evidence from three decades of research combining various observables reveals the effects of the produced QGP medium. Whilst somewhat context-dependent, the following features make QGP the most extreme phenomena observed phenomena in terms of its:

- *Temperature*: QGP temperatures reach values on the order of hundreds of MeV, which corresponds to approximately 2×10^{12} K.²
- *Viscosity*: the shear viscosity to entropy density ratio η/s reaches the minimum quantum limits of $1/4\pi$, making it an almost perfect liquid.
- *Vorticity*: in semi-peripheral collisions, the rotating plasma reaches a vorticity parameter of approximately 0.4 fm^{-1} .
- *Magnetic field*: in non-central collisions, the magnetic fields of the heavy nuclei may peak at $\sim 10^{19} \text{ T}$.

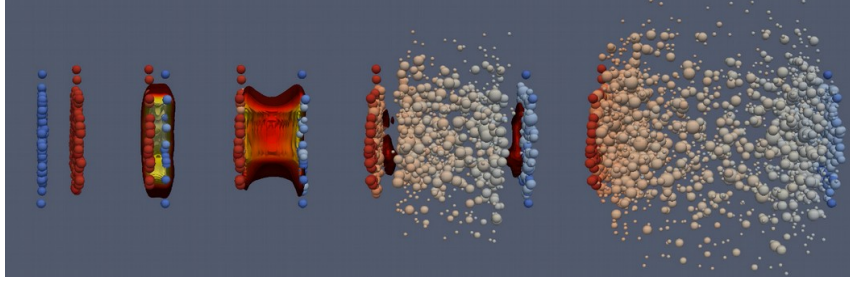


Figure 2.2: TBA

Figure 2.2 illustrates the mainstream paradigm of a heavy nuclei collisions evolution:

1. The Lorentz-contracted heavy nuclei approach each other at ultra-relativistic speeds.
2. *Pre-hydrodynamisation stage* ($\tau \equiv \sqrt{t^2 - z^2} \leq 1 \text{ fm/c}$): “hard” particles are produced in scatterings with the highest momentum transfer Q^2 , produced matter expands rapidly in longitudinal directions and starts expanding in radial direction.
3. *Hydrodynamisation* ($1 \leq \tau \leq 10 \text{ fm/c}$): partons are abundantly produced, creating a deconfining medium and allowing the system to be described by hydrodynamic equations.

²Contrasting some of the lowest temperatures required for the super-conducting magnets of the LHC, $T \approx 1.9 \text{ K}$.

4. *Chemical freeze-out* ($\tau \sim 20$ fm/c): the cools down, hadronises, produced hadrons then stop interacting inelastically and the system's chemical content is stabilised.
5. *Thermal freeze-out*: hadrons no longer interact elastically and their kinematics stabilize.

The following subsections outline some of the essential phenomena related to the production of QGP.

2.2.1 Quarkonium dissociation and sequential suppression

Heavy quarkonia are vector mesons of $c\bar{c}$ and $b\bar{b}$. They include J/ψ , $\psi(2S)$, $\Upsilon(1S)$, $\Upsilon(2S)$, $\Upsilon(3S)$, which can be relatively easily measured in LHC experiments via their di-lepton decay channels. They are created solely in the first phases of the collision and then experience the entire evolution of the QGP medium:

$$t_{\text{creation}}^{Q\bar{Q}} < t_{\text{creation}}^{\text{QGP}} < t_{\text{lifetime}}^{\text{QGP}} \ll t_{\text{lifetime}}^{Q\bar{Q}} \quad . \quad (2.2)$$

Additionally, due to their large binding energies, their radii may remain smaller than the plasma screening radius $r_D(T)$, and thus, survive the dissociation. For instance, considering their in-vacuum radii determined from the $q\bar{q}$ potential, $r_{\Upsilon(1S)} \sim 0.14$ fm, $r_{\Upsilon(2S)} \sim 0.28$ fm, $r_{\Upsilon(3S)} \sim 0.39$ fm, which contrast the $r_\pi \sim 0.7$ fm. This implies that different temperatures result in the dissociation of different states, and measuring the production of different states can help infer QGP temperature, as illustrated in Fig. 2.3.

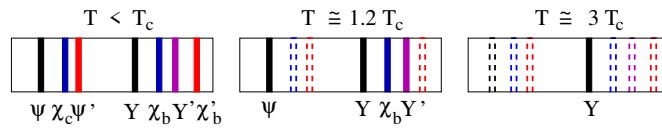


Figure 2.3: TBA

The production of heavy quarkonia in AA collisions is compared to that in pp collisions through the nuclear modification factor, R_{AA} . This factor is widely used in various other AA measurements and is defined as:

$$R_{AA} = \frac{dN_{AA}/dp_T}{\langle N_{\text{coll}} \rangle dN_{pp}/dp_T} \quad . \quad (2.3)$$

R_{AA} can take on the following values:

1. $R_{AA} = 1$: There is no net effect on the production, corresponding to the absence of the QGP medium and other nuclear effects.
2. $R_{AA} < 1$: The production is overall suppressed, for example, due to dissociation.
3. $R_{AA} > 1$: The plasma and nuclear effects systematically enhance the measured production.

At LHC energies, the abundance of charm quarks in the QGP is high enough that charmonia can be reformed after dissociation, which somewhat complicates the interpretation of their suppression. However, the $\Upsilon(3S)$ bottomonium has R_{AA} consistent with 0 at $\sqrt{s_{NN}} = 5.02$ TeV, as shown in Figure 2.4. This complete suppression is a clear signature of the QGP and can be used together with models to estimate the QGP temperature at these energies as $T \approx 630$ MeV.

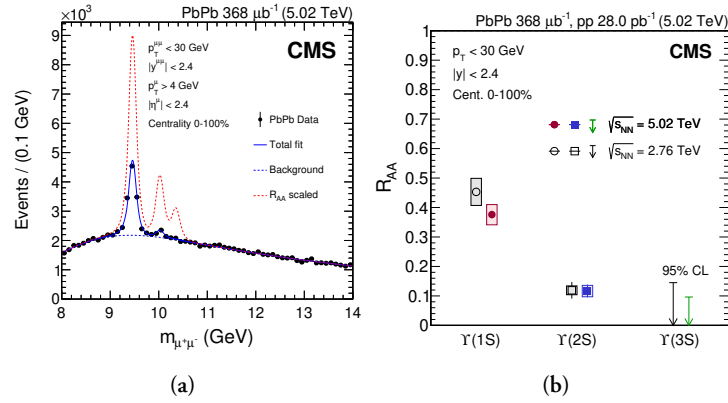


Figure 2.4: TBA

2.2.2 Strangeness enhancement

TBA

2.2.3 Collective flow

TBA

2.2.4 Jet quenching

TBA

2.2.5 Cold nuclear matter effects

It should be noted that apart from the QGP, other effects come into play due to the fact that the collision involves two nuclei instead of two protons. These effects are important caveats to bear in mind and include:

1. Nuclear (anti-)shadowing: Reflects the modification in production due to differences in nPDFs and PDFs.
2. Cronin effect: Describes the initial parton energy loss due to scatterings in the nuclear medium and broadens measured p_T spectra.
3. Nuclear absorption: Describes the dissociation of particles due to their interactions with the passing-by nuclear remnants. It is generally negligible at LHC energies.
4. Co-mover absorption: This is the effect of inelastic interactions with the hadron gas.

These effects can be isolated and quantified in pA or very peripheral AA collisions.

2.3 QGP phenomena in small systems

Measurements within the last decade have shown that certain QGP phenomena can also be observed in high-multiplicity events of pp collisions at LHC energies, which challenges the traditional assumption that QGP is only produced in AA collisions. This has sparked debates about the existence of QGP in pp collisions and, to a lesser degree, about the absence of QGP in AA collisions, despite the extensive experimental evidence.

Furthermore, the observed behavior of these phenomena indicates that the role of event multiplicity N_{ch} may be more significant than system size. This has led to ongoing efforts to establish a consistent and seamless link between the paradigms of pp and AA collisions.

Strangeness and charm enhancement

ALICE measurements on Λ/π , Ξ/π , and Ω/π ratios demonstrate that the production rates of particles containing strange quarks increase faster with multiplicity than those containing only u and d quarks. This also depends on the strangeness content – the effect is the strongest for Ω and vanishes for protons. Furthermore, the evolution to larger systems seems to be continuous with respect to N_{ch} . The measurements can be seen in Fig. 2.5.

To contrast the strangeness measurements with heavier flavour, the $J/\psi/\pi$ ratio also shows a clear increase in yield with increasing N_{ch} in pp collisions, as is shown in Fig. 2.5. However, this comes with an important caveat: high-multiplicity events are biased to have enhanced hard processes, as discussed further in Chapter X. Moreover, the evolution of this phenomenon is also not continuous with N_{ch} when going from pp collisions at $\sqrt{s} = 13$ TeV to $\sqrt{s_{\text{NN}}} = 5.02$ TeV, which can also be explained by the fact that charm quarks are produced solely in hard scattering processes, the rates of which depend on the collision system and center-of-mass energy.

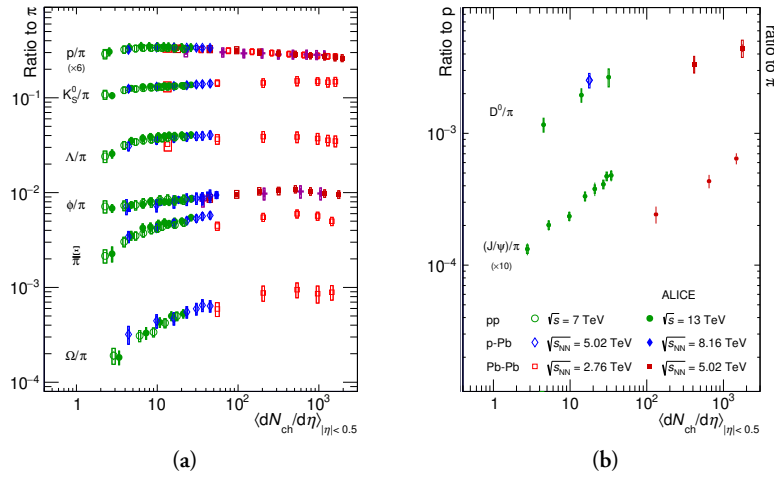


Figure 2.5: TBA

Anisotropic flow

Azimuthal correlations and anisotropic flow measurements in small collision systems exhibit features similar to those observed in AA collisions, hinting at the presence of collective expansion. However, in small systems, these measurements are particularly challenging due to their large sensitivity to non-flow effects, such as jet fragmentation or resonance decays, which can mimic the features of collective flow.

While models using hydrodynamic-like descriptions seem to be able to describe the data, especially at high multiplicities, the interpretation of the results in small systems is still under investigation. The values of elliptic flow v_2 seem to be comparable to those in low-multiplicity Pb-Pb collisions, although the evolution of v_2 across different system sizes does not appear to be smooth. The measurements from CMS displaying a clear ridge in high-multiplicity events and the v_2 results from ALICE can be seen in Fig. 2.6.

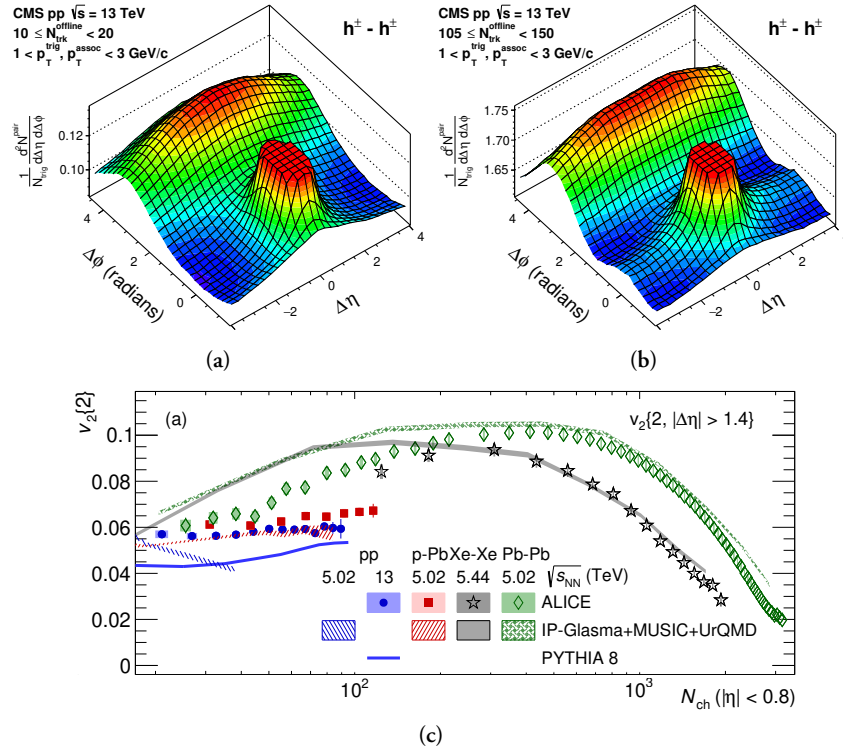


Figure 2.6: TBA

Radial flow

Measurements of the ratio of Λ to K_S^0 p_{T} spectra ratio were also studied in pp collisions with differing N_{ch} . The boost of a collectively expanding system, as expected in the context of radial flow, should have a greater impact on heavier hadrons, leading to an enhancement of the baryon-to-meson ratio at intermediate p_{T} . This enhancement is observed in the $(\Lambda^0 + \bar{\Lambda}^0)/(2K_S^0)$ ratio, its magnitude increases with increasing N_{ch} and the peak position shifts towards higher values collisions, consistent with the

hydrodynamic picture. The increase at intermediate momenta leads to a corresponding depletion at low p_T . Integrated (or high- p_T) $(\Lambda^0 + \bar{\Lambda}^0)/(2K_s^0)$ ratios exhibit essentially no (or minor) multiplicity dependence. This observation also applies to proton-to-pion ratios.

Recent studies have also investigated the charmed baryon-to-meson ratio Λ_c/D^0 , with similar findings, although measurements with smaller uncertainties are still required. Fig. 2.7 presents the corresponding results.

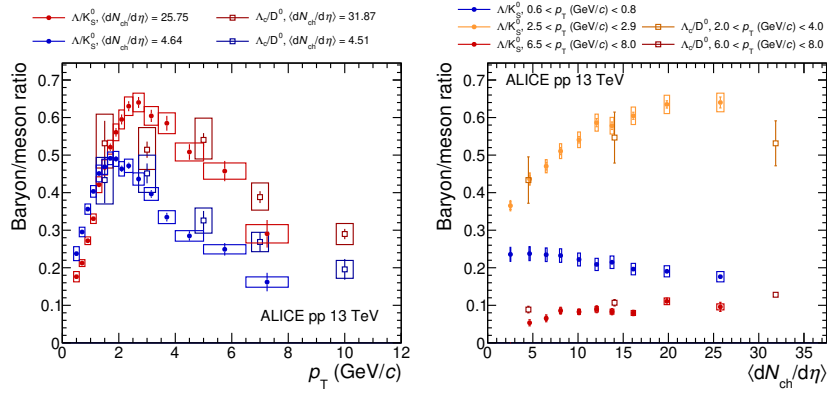


Figure 2.7: TBA

Sequential suppression of Υ states

While defining R_{AA} to compare high-multiplicity and low-multiplicity events is unclear, and measuring yields as a function of N_{ch} is complicated by its biases related to the hardness of primary scatterings, it is worthwhile to investigate the ratio of excited-to-ground states of quarkonia as a function of N_{ch} .

Interestingly, these results exhibit a decrease with increasing N_{ch} , resembling the pattern of sequential suppression due to QGP deconfinement. Even more remarkable, this dependence disappears in low-sphericity, jet-dominated, events (event shape observables such as sphericity are discussed in more detail in Chapter X). These findings, reported in Fig. 2.8, suggest that the dependence on N_{ch} is solely influenced by the UE, rather than jets. As event multiplicity grows larger, excited Υ states become relatively less likely to be measured compared to the ground state.

These results indicate the need for a better understanding of Υ hadronization and the role UE may play in it. They also raise the question of whether the ground state is enhanced rather than the excited states being suppressed. Additionally, the effects of

the mass differences must also be considered. However, the fact that low-sphericity, jet-dominated events have the same ratios as high-sphericity, UE-dominated events at low N_{ch} argues against these ideas.

An important caveat to note is that hadronic decays (which are dominant) of the heavy Υ states may result in tens of produced N_{ch} . Therefore, even minor discrimination against the excited states could hypothetically be correlated with a substantial but trivial increase in the accompanying N_{ch} . To the author's knowledge, there are currently no available phenomenological descriptions of the observed behavior, which further limits potentially groundbreaking interpretations.

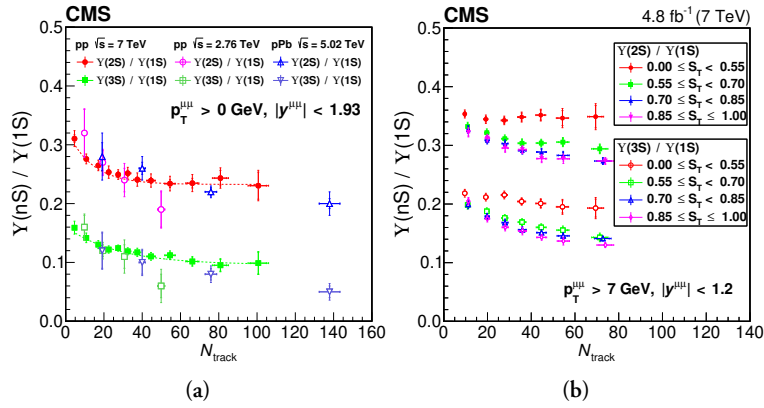


Figure 2.8: TBA

Other QGP signatures

Jet quenching

2.3.1 Role of multiplicity

The observations made above highlight the significance of studying the role of multiplicity N_{ch} . In contrast to AA collisions, high-multiplicity events in pp collisions do not arise from a mere increase in the amount of colliding matter, as the values of N_{part} and N_{coll} are fixed:

$$N_{\text{part}} = 2, \quad N_{\text{coll}} = 1. \quad (2.4)$$

Additionally, due to the relatively constant initial system volume, high- N_{ch} pp events may exhibit energy densities that exceed the threshold for QGP formation, given that

the highest N_{ch} values are similar to those observed in peripheral AA collisions, where QGP formation is observed.

Clearly, the picture is more complex and despite its simplicity as an event activity classifier, N_{ch} poses challenges when it comes to relating data to theory since it cannot be directly linked to the initial state, and multiplicities in different events may originate from entirely different processes.

To address these issues and gain a better understanding of the evolution between low and high multiplicities and the potential for QGP formation, this dissertation focuses on transverse sphericity $S_{\text{O}}^{(p_{\text{T}}=1.0)}$ and underlying event activity R_{T} measurements. They may offer a deeper insight into the relevant degrees of freedom involved.

2.4 Multiple partonic interactions

2.4.1 Color reconnection

2.5 Underlying event

2.6 Phenomenological models

2.6.1 Pythia

Ropes

2.6.2 Epos LHC